Nanoscale

Floating Gate Negative Capacitance MoS2 Phototransistor with High Photosensitivity

Journal:	*Nanoscale*
Manuscript ID	NR-ART-09-2021-006315.R1
Article Type:	Paper
Date Submitted by the Author:	24-Dec-2021
Complete List of Authors:	Nur, Roda; The University of Tokyo, Tsuchiya, Takashi; National Institute for Materials Science, International Center for Materials Nanoarchitectonics Toprasertpong, Kasidit; The University of Tokyo Terabe, Kazuya; National Institute for Materials Science (NIMS), WPI Center for Materials Science Nanoarchitectonics (MANA) Takagi, Shinichi; The University of Tokyo Takenaka, M.; The University of Tokyo

Title Floating Gate Negative Capacitance MoS_2 Phototransistor with High Photosensitivity

Roda Nur, Takashi Tsuchiya, Kasidit Toprasertpong, Kazuya Terabe, Shinichi Takagi, and Mitsuru Takenaka*

R. Nur, Prof. Kasidit Toprasertpong, Prof. Shinichi Takagi, Prof. Mitsuru Takenaka
7-3-1 Hongo, Bunkyo-ku, Tokyo113-8656, Japan
E-mail: nur@mosfet.t.u-tokyo.ac.jp

Dr. T. Tsuchiya, Dr. K. Terabe
International Center for Materials Nanoarchitectonics, National Institute for Materials Science (NIMS), 1-1 Namiki Tsukuba, Ibaraki 305-0044, Japan

Keywords: MoS_2, Ferroelectric, Phototransistor, Photogating, Floating gate

Monolayer MoS_2 exhibits interesting optoelectronic properties that have been utilized in applications such as photodetectors and light emitting diodes. For image sensing applications, improving the light sensitivity relies on achieving a low dark current that enables the detection weak light signals. Although previous reports to improve the detectivity have been explored with heterostructures and pn junction devices, some these approaches lack CMOS compatibility processing and not sufficiently low dark current suppression. Steep slope transistors that overcome the Boltzmann tyranny can further enhance the performance in photodetectors by providing efficient extraction of photogenerated charges. Here, we report a monolayer MoS_2 floating gate negative capacitance phototransistor with the integration of a hafnium-zirconium oxide ferroelectric capacitor. In this study, a SS_{min} of 30 mV/dec, very low dark currents 10^{-13}~10^{-14}A, and a high detectivity of $7.2x10^{15}$ cm $Hz^{1/2}$ W^{-1} was achieved under weak light illumination due to an enhancement in the photogating effect. In addition, its potential as an optical memory and as an optical synapse with excellent long-term potentiation characteristics in an artificial neural network were also explored. Overall, this device structure offers high photosensitivity of weak light signals for future low-powered optoelectronic applications.

1. Introduction

Photodetectors are used in various applications such as image sensing, surveillance, and biomedical imaging[1,2]. Research efforts have been focused towards exploring materials and device structures to improve the incident light absorption and conversion efficiency into current. 2D materials are particularly promising due to their interesting optoelectronic properties[38,39,40] and thus have been applied to phototransistors where the built-in electric field generated can enable efficient photocarrier extraction. An n-type and p-type MoS_2 phototransistor based on a PN junction achieved a high responsivity of $7x10^4$ A/W and a detectivity of $3.5x10^{14}$ Jones[3]. Modifying the Schottky barrier in graphene/MoS_2 heterojunctions was explored where a high responsivity and detectivity of $2.2x10^5$ A/W and $3.5x10^{13}$ Jones respectively was demonstrated[4]. Pb quantum dots integrated with MoS_2 have also been demonstrated to enhance the photosensitivity via interface engineering to improve the I_{on}/I_{off} ratio[5]. Further improvement in the detectivity can enable the detection of weak light signals that could not be detected leading to better imaging resolution for applications like facial recognition and surveillance systems. In addition, for the practical integration of highly photosensitive detectors in imaging sensing technologies, it is important to have a complementary-metal-oxide-semiconductor (CMOS) compatible processing and low power operation.

Steep slope transistor device structures that overcome the Boltzmann tyranny have a promising potential in photodetection applications. The subthreshold swing (SS) is defined as the amount of gate voltage (V_G) required to increase the drain current (I_{DS}) by one decade.

$$SS \equiv \frac{dV_G}{dlog_{10}[I_{DS}]} = \left[\frac{dV_G}{d\varphi_s}\right]\left[\frac{d\varphi_s}{dlog_{10}[I_{DS}]}\right] = \left[1+\frac{C_s}{C}\right]\left[\frac{k_T}{q}\ln(10)\right] = m \times n$$

, where C_s is the semiconductor depletion capacitance, C is the gate insulator capacitance, and φ_s is the channel's surface potential. The limiting factor in scaling SS in conventional field effect transistors (FET) comes from the carrier transport (n) term. Here, the SS can be scaled down to a minimum of 60 mV/dec due to the Boltzmann factor (kT/q) at room temperature conditions. There are two approaches to reduce the SS which is either modifying the carrier transport (n) in the channel region like tunneling FETs or by changing the gate capacitance (m). Ferroelectrics are nonlinear insulators that have two remnant polarization states that can be retained without the application of an applied electric field. Negative capacitance FETs using ferroelectric insulators can reduce the body factor (m) to values less than 1 offering sub 60 mV/dec SS[6]. An attractive feature of a negative capacitance device structure is that it allows for the flexibility in changing the photoactive channel material and its structure does not impact the carrier transport physics. A previous study explored the application of multi-layered NC MoS_2 phototransistors using capacitance matched hafnium-zirconium oxide (HZO)/Al_2O_3 gate stack where they achieved an impressive steep subthreshold slope 17.64 mV/dec and a detectivity of 4.75×10^{14} cm $Hz^{1/2}$ W^{-1} at an effective optical power of 2.7 nW with the photogating effect[7]. Although the photogating effect can offer higher photocurrents due to its charge trapping mechanism, a limitation of its sensitivity arises from the fixed density of oxide traps in the dielectric layer. Under the illumination of different light intensities, the filling of oxide trap sites by photogenerated minority carriers will reach saturation. This results in limited threshold voltage shifting which directly impacts its photosensitivity. In order to further improve the light sensitivity with the photogating effect via higher threshold voltage shifting, the use of materials with more charge trapping storage capacity is needed.

In this work, we explore for the first time monolayer MoS_2 negative capacitance floating gate (NCFG) phototransistors by using a series connection of an HZO ferroelectric capacitor with a conventional ZrO_2 MoS_2 phototransistor. According to NC theory, during the state-to-state transition from polarization switching, the ferroelectric capacitor provides a brief transient negative capacitance that couples to the positive capacitance in the conventional FET device which should provide a low SS and lower power consumption. However, due to the inherent floating metal gate in this device structure, it can also function as a floating gate memory device to further enhance the hole-trapping from the photogating effect. As a result, we obtained an enhancement in the photogenerated hole-tunneling into both oxide traps in ZrO_2 and the TiN floating gate. This combined effect provided strong threshold voltage shifting for weak optical powers. The highest detectivity among various types of MoS_2 photodetectors was achieved with peak value of $7.2\text{x}10^{15}$ cm $Hz^{1/2}$ W^{-1}. An SS_{min} of 30.2 mV/dec and low dark currents in the range of 10^{-13}~10^{-14} A were also obtained. Moreover, due to the long carrier lifetime from hole de-trapping, optical memory functionality such as multi-level state programming and charge retention was measured under weak optical power densities. In addition, its potential as an optical synapse in an artificial neural network was also evaluated. Overall, this NCFG device structure shows a promising practical option to develop high sensitivity 2D photodetectors for low power and weak light detection.

2. Results and Discussion

2.1. Device Structure and MoS_2 Characterization

The device structure of the monolayer MoS_2 NCFG phototransistor can be found in **Figure 1a**. The NCFG structure was composed of HZO with top and bottoming capping layers of TiN. The film thicknesses from bottom to top was TiN (50 nm)/HZO (11 nm)/TiN (30 nm). TiN was deposited by DC sputtering, and HZO was deposited by atomic layer deposition (ALD). After the TiN capping of HZO, a rapid thermal annealing (RTA) was performed to produce ferroelectricity behavior. Next, 11 nm of ALD ZrO_2 was deposited as the dielectric layer. Chemical vapor deposition (CVD) monolayer MoS_2 was transferred, and then source-drain contacts of 10 nm Ti and 70 nm Au was deposited by e-beam evaporation. More details can be found in the Experimental Methods section. A close-up image of the channel region is in Figure 1b, where the dotted box emphasizes the location of the MoS_2 flake. The channel length of the devices in this study were ~2.5 μm. A Raman characterization was performed to confirm the transferred monolayer film onto the ZrO_2 dielectric layer. As seen in Figure 1c, the measured Raman shift was 19.8 cm^{-1}. As a reference, a Raman shift of around 19 cm^{-1} corresponds to monolayer MoS_2[8].

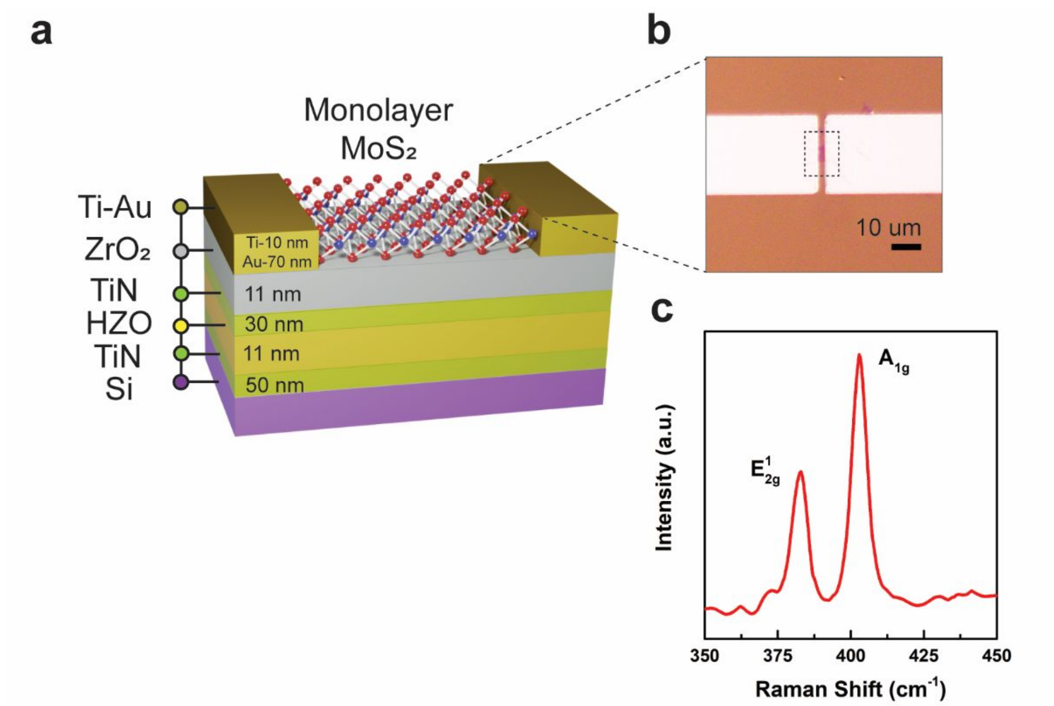

Figure 1. a) Device structure of negative capacitance floating gate (NCFG) monolayer MoS_2 phototransistor. b) Image of channel region where the dotted box shows the location of MoS_2. The scale bar is 10 μm. c) Raman spectrum of transferred monolayer MoS_2 with a Raman shift of 19.8 cm^{-1}.

2.2. Ferroelectricity and Negative Capacitance Effect

The observation of ferroelectricity in HfO_2 films doped with elements such as Si[9], Zr[10], Y [11], and Al[12] has been reported. In comparison to other ferroelectric materials like lead based PZT[13] and organic polymers like PVDF[14], ALD doped-HfO_2 is a promising option for the development of ferroelectric devices due to its decent remnant polarization (10~45 $\mu C/cm^2$) for small film thicknesses (< 10 nm) and its CMOS compatible processing.

The driving force for ferroelectricity in doped-HfO_2 films has been attributed to the formation of the non-centrosymmetric orthorhombic phase ($Pbc2_1$) from tensile stresses induced from a capping layer [9]. TiN capping with HZO is one of the most studied metal/ferroelectric/metal (MFM) structures and has been shown to offer high polarization values around a film thickness of 10 nm[10,15,16]. In this study, a MFM capacitor structure as seen in **Figure 2a** was fabricated. To obtain a high remanent polarization (P_r), different post-metallization annealing (PMA) temperatures were analyzed. The best result was at a PMA of 700°C and its measured polarization as a function of applied electrical field (P-E) at 1 kHz is in Figure 2b. The P_r was 22 $\mu C/cm^2$ and the coercive field (E_c) was 1.3 MV/cm. Its capacitance-voltage characteristics can be seen in supporting information fig. 1.

The negative capacitance concept is understood from the energy landscape of a ferroelectric capacitor that is modelled by a double well that has two energy minimums which represents the two polarization states (Figure 2c). From the Gibbs free energy for ferroelectrics:

$$U = \alpha P^2 + \beta P^4 + \gamma P^6 + EP \qquad (1)$$

U is the energy, P is the polarization, and E is the electric field. The static Landau coefficients of α, β, and γ are material-related parameters. For ferroelectric materials $\alpha < 0$.

The time-dependent Landau-Khalatnikov (LK) equation:

$$dU/dP + \rho dP/dt = 0 \qquad (2)$$

can be applied to obtain a relationship between the polarization and applied electric field where under steady-state conditions $dP/dt = 0$:

$$E = 2\alpha P + 4\beta P^3 + 6\gamma P^5 + \rho dP/dt \qquad (3)$$

A fitting of the LK model to the P-E measurement can be seen as the orange curve in Figure 2b. The α, β, and γ coefficients from the fitting were -5.5×10^8 Vm/C, 4.8×10^9 Vm^5/C^3, and 1.2×10^{10} Vm^9/C^5 respectively. The negative capacitance effect arises from the region in the

P-E characteristics where the slope (dP/dE) is negative as seen by the LK curve in the middle segment of the P-E measurement. This region occurs between the polarization state-to-state transition. The capacitance of a ferroelectric capacitor can be determined from equation 1:

$$C_{FE} = [d^2U/dP^2]^{-1} \quad (4)$$

With the series connection of two positive capacitors, the equivalent capacitance is generally lower than the smallest capacitance value. A schematic of the negative capacitance transistor with its capacitors and node voltages are seen in Figure 2d. Although the negative capacitance state is unstable, it can be partially or fully stabilized by a series connection with a positive capacitor. Under the NC regime, C_{FE} is negative and C_{ox} is positive. As a result, the total gate capacitance becomes larger resulting in the internal amplification of the channel's surface potential for smaller V_G biasing[6]. This NC effect was proposed to have the potential to achieve a steep SS with the attractive feature that the transport physics of the device remain unaltered.

To test the potential of the internal voltage amplification gain ($\delta V_{int}/\delta V_G$), an MFMIM structure (inset of Figure 2b) was measured. The measurement involved sweeping the gate voltage and measuring the floating potential of TiN under a zero current bias. The amplification gain factor for both the forward and reverse scans can be seen in Figure 2b. It displayed a transient amplification gain where the peaks of the forward and reverse gains were 3.79 and 2.31 respectively. The transfer characteristics of the ferroelectric driven NCFG phototransistor under the dark condition (no light illumination) can be found in Figure 2e at V_{DS} = 100 mV. This device displayed a small hysteresis window of 0.35V, a forward threshold voltage V_{TH} of 0.5 V, an I_{on}/I_{off} ratio of 6.6x10^6, and a low I_{off} in the range of ~10^{-14}A. A sub 60 mV/dec SS was observed in the lower subthreshold region where the gate leakage current exceeds the drain current. This behavior of $I_G > I_D$ in this region can also be seen in a similar device structure using HfO_2 as the dielectric layer[32]; however, they achieved a steep SS as I_D became larger than I_G. Although most NC devices have claimed sub

60 mV/dec SS over multiple current decades, they have not provided detailed discussion that the gate current contribution in this lower SS region can cause the drain current to increase rapidly, thus yielding misleading SS values. In order to evaluate the true SS_{min} without the gate current contribution in this region, an approximation method found in supporting information fig. 2 was used. In Figure 2f, it shows the subthreshold swing as a function of the drain current where the forward SS_{min} was 30.2 mV/dec. According to the quasi-static NC theory that was previously discussed, a stabilized NC effect from capacitance matching should produce hysteresis-free I-V. However, for this device, hysteretic behavior was observed and the sub-60 mV/dec SS occurred only in the forward sweep which aligns with the forward scan transient voltage amplification gain. The transfer characteristics showed a clockwise hysteresis loop indicating the presence of electron trap sites near the conduction band edge of MoS_2 most likely due to presence of ambient gases and absorbates from the exposed channel. As a result, the reverse curve does not coincide with the reverse amplification gain, thus resulting in a higher SS. It is most likely that this device displays transient NC effects due to the transition in polarization switching in the ferroelectric layer.

A feature of NCFETs is the observation of negative differential resistance (NDR) in the output characteristics due to the coupling of the drain voltage (V_D) and the internal gate voltage (V_{int}). Drain-Induced Barrier Lowering (DIBL) is an undesirable short-channel effect where at larger V_D, the barrier height between the source and drain gets lowered where both the gate and drain voltages control the channel. For NCFETs, the internal gate voltage is a function of the gate and drain voltage:

$$V_{int} = \frac{|C_{FE}| \times V_G}{|C_{FE}| - C_{MOS}} + \frac{-C_{GD} \times V_D}{|C_{FE}| - C_{MOS}} = A_G \times V_G + [-A_D \times V_D] \qquad (5)$$

where C_{FE} is the ferroelectric capacitance, C_{MOS} is the total underlying transistor capacitance, A_G is the voltage amplification gain, and A_D is the drain coupling factor. Although V_G is held constant, V_{int} changes due to the gate-to-drain capacitance coupling. Initially, V_{int} is high when $V_D = 0V$; however, as V_D increases, V_{int} drops resulting in a reduction of the gate charge[17,18]. In the saturation region of the output characteristics where V_G is constant and V_D is increasing, a decrease in the channel current can be observed. The output characteristics in Figure 2g displayed a peaking of the drain current followed by a decrease with increasing V_D. At lower V_D as seen in supporting information 3, linear output curves were measured indicating ohmic-like contacts to MoS_2. In supporting information fig. 4, I_D-V_D was measured under different voltage sweeps with another device which also displayed this NDR effect. For comparison, conventional FET device structures of back-gated Si-ZrO_2 and Si-TiN-ZrO_2 were also measured where its output characteristics can be found in supporting information fig. 5 and fig. 6, respectively. Their output characteristics did not display this NDR effect. The transfer characteristics of the Si-ZrO_2 and Si-TiN-ZrO_2 are seen in supporting information fig. 7 and 8 respectively. The high gate current leakage in the Si-ZrO_2 can be attributed to the preferred tetragonal phase crystal growth on the silicon back gate in comparison to the TiN-ZrO_2 (supporting information fig. 9).

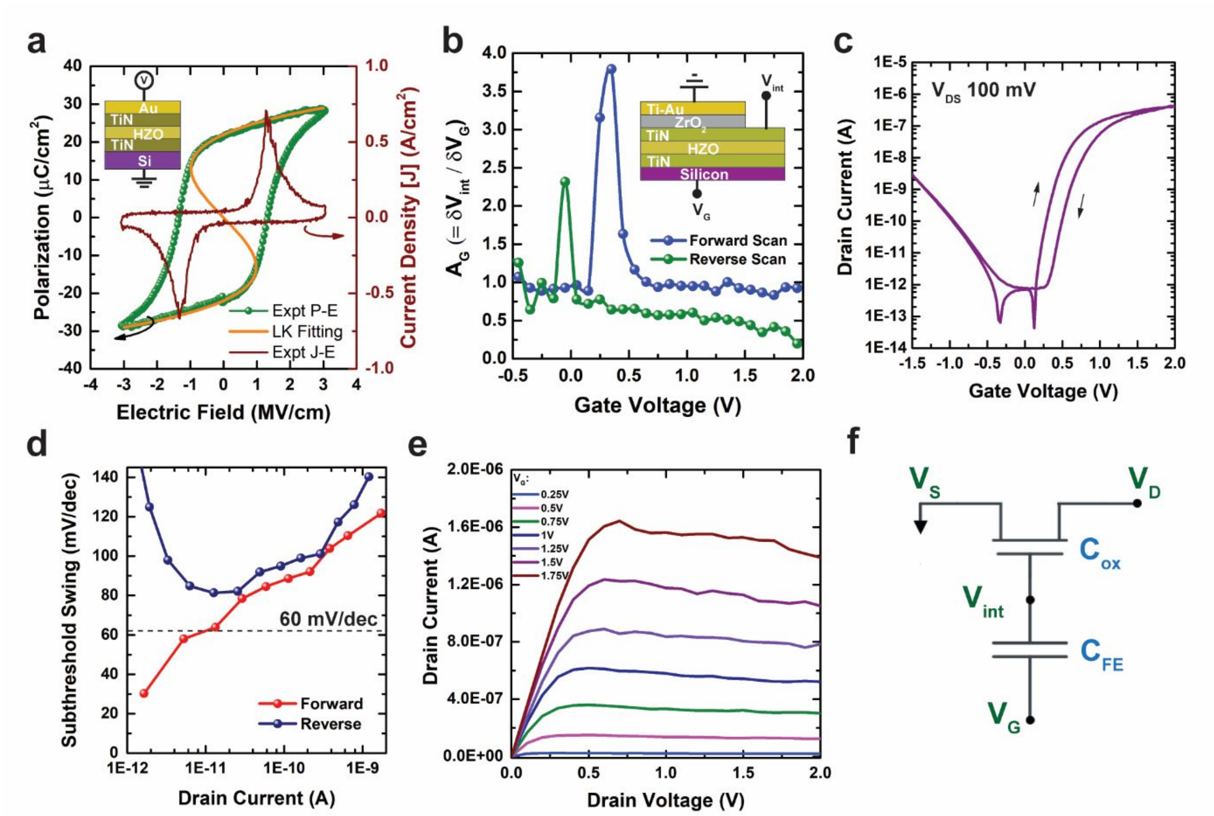

Figure 2. a) Structure of metal-ferroelectric-metal (MFM) capacitor (inset image). P-E measurement of MFM capacitor at 700°C annealing at 1kHz (green line). L-K fitting to the measurement is plotted in orange. Current density is the red plot (right side). b) Voltage amplification of the gate stack. c) Transfer characteristics of the NCFG phototransistor under dark condition. d) Subthreshold swing as a function of drain current. e) Output characteristics under dark condition. f) Device schematic of negative capacitance floating gate (NCFG) phototransistor with capacitors and voltage nodes.

2.3. Photoresponse

The photoresponse of the NCFG phototransistor was evaluated with green light illumination (λ= 515 nm) and under ambient conditions. As previously mentioned, low light intensities in the range of P_{eff} = 1.4 fW to 6.3 pW for the effective light powers was studied to characterize its sensitivity to low light detection. **Figure 3a** shows the photoresponse of the NCFG device biased under V_{DS} = 100 mV. The strong parallel shifting of the illumination curves indicates that the dominating photocurrent generation comes from the photogating effect. The photogating effect relies on the trapping of the photogenerated holes at the dielectric/semiconductor interface, which results in developing a local built-in electric field that shifts the Fermi level to induce more electrons.[19,20,42] In addition, to evaluate the enhancement in photodetection with the NCFG device structure, a conventional back-gate TiN-ZrO_2 and Si-ZrO_2 device were measured and their photoresponse results can be found in Figure 3b,c respectively. The Si-ZrO_2 device structure showed higher gate leakage current due to the polycrystalline structure from the as-deposited ZrO_2 resulting in a higher I_{off}. In addition, its light curves showed weak detection of low optical power densities. With the TiN-ZrO_2 device, it showed lower gate leakage current due to the suppression of the tetragonal (111) crystal phase in comparison to the Si-ZrO_2 device structure leading to a lower I_{off}. The incorporation of the TiN metal back gate provided an improvement in detecting the same optical power densities. The NCFG device was able to better detect the lowest optical power density of 1.19 μW/cm^2 in comparison to the other device structures which either could not detect (Si-ZrO_2) or could detect weakly (TiN-ZrO_2). In Figure 3d, it shows the change in the threshold voltage from light illumination under varying optical power densities where $\Delta V_{TH} = V_{LIGHT}-V_{DARK}$. The observation of threshold voltage shifting is a method of confirmation of the presence of photogating. This plot shows the result from all 3 device structures where the NCFG device showed overall the greatest amount of threshold voltage shifting. The maximum change in the threshold voltage shifting was -0.92 V for 51.8 μW/cm^2 which is quite a low light intensity in comparison to other MoS_2 phototransistors that have investigated photogating at higher optical powers.[7,20,21,22]

The photodetection mechanism for this device relies on the photogating effect. We have previously studied high-k metal oxide dielectric HfO_2 with multi-layered MoS_2 and found the photogating effect was a dominating photocurrent generation mechanism.[30] This was due to the valence band maximum (VBM) of MoS_2 having good band edge alignment with the intrinsic oxygen vacancies of HfO_2. For ZrO_2, it also has oxygen vacancy point defects located within its bandgap which serve charge-trapping sites[23,24]. Even without the presence of light irradiation, electrical stress biasing can also induce charging effects into

ZrO_2 where holes can be injected. [25] The photogenerated hole trapping at the MoS_2/ZrO_2 interface most likely occurs via charge tunneling from the VBM alignment of MoS_2 to these oxide defect energy levels. In addition, the presence of ambient gases and absorbates that are known to deplete the MoS_2 channel can also serve as an additional source of charge-trapping sites[26,41].

With the integration of a ferroelectric capacitor to a high-k 2D FET, it contains a floating gate (TiN) that can serve as an additional charge-trapping storage layer. During the photogenerated carrier extraction process in MoS_2, the photogenerated holes can tunnel into ZrO2 via oxygen vacancy point defects due to its VBM alignment. Due to the intrinsic fixed defect density in ZrO_2, additional photogenerated holes can tunnel into the TiN floating gate due to the enhancement of the electric field generated from the transient voltage amplification. This enhanced photogating effect was more pronounced in the NCFG device structure in comparison to the conventional Si-ZrO_2 and TiN-ZrO_2 devices which represents the case of a non-floating gate/ferroelectric device. An overview of this photogating mechanism process can be seen in Figure 3e which shows the movement of the photogenerated hole carriers. Evidence of hole-trapping can be indirectly observed in the gate current where an enhancement in the electron leakage current results from a barrier lowering effect from the hole-trapping into an oxide layer[34]. In supplementary figure 10, it shows the gate current in ZrO_2 as a function of the gate voltage for the NCFG and TiN-ZrO_2 devices under the dark condition and illumination. The hump observed in the illumination curves corresponds to the enhanced electron tunneling due to the photogenerated hole-trapping in ZrO_2. Overall, the NCFG structure showed more pronounced humps indicating there is more hole-trapping in this device structure under illumination.

The NCFG photocurrent generation was also evaluated. The photocurrent as a function of V_G can be seen in supplementary figure 11. At V_G = 0.7 V which is 0.2 V above its dark V_{TH}, this device displayed peak photocurrents ranging from 1.8x10^{-8} A to 1.6x10^{-7} A. The I_{PH}/I_{DARK} ratio was as high as 2x10^{6} for V_G = 0.125V at optical power density 51.8 μW/cm^2. Lastly, the relationship between the photocurrent and optical power density can be seen in Figure 3f under different gate biasing conditions: 0.125 V for depletion mode, 0.7 V slightly above V_{TH} and around the peak photocurrent generation, and 1.2 V for accumulation mode operation. All of these curves showed a non-linear photocurrent dependence on the optical power density indicating that there is a presence of traps and complicated photocarrier generation processes[27].

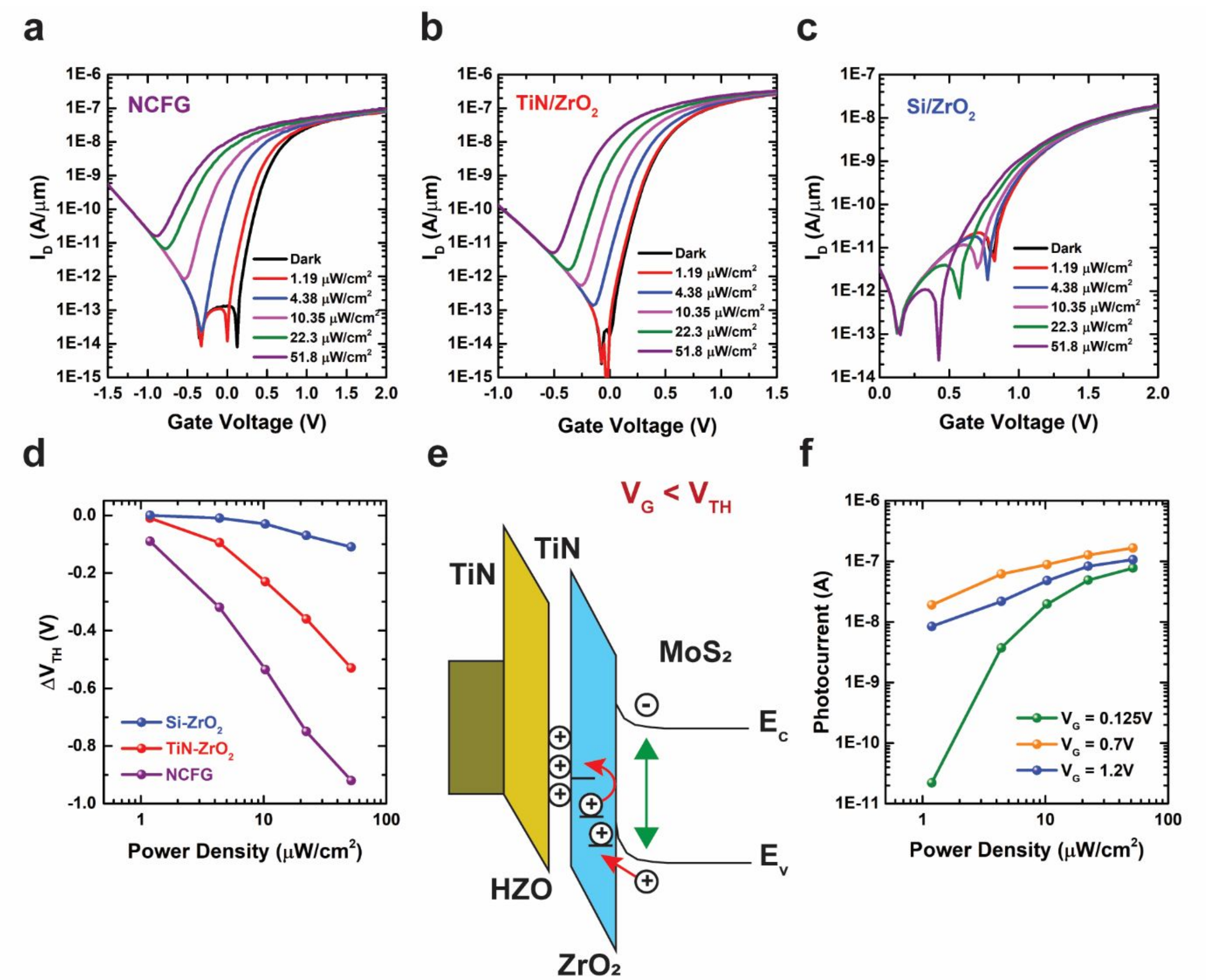

Figure 3. a) Photoresponse of NCFG phototransistor under green light illumination and V_{DS} at 100 mV. b) Photoresponse of monolayer TiN-ZrO_2 (conventional FET) phototransistor. c) Photoresponse of monolayer Si-ZrO_2 (conventional FET) phototransistor. d) Threshold voltage shift from illumination at different optical power densities for NCFG (purple), TiN-

ZrO_2 (red), and Si-ZrO_2 (blue). e) Mechanism of the photogating effect with the photogenerated hole-trapping into ZrO_2 and in the TiN floating gate. f) Photocurrent as a function of optical power density at different gate voltage biasing showing sublinear dependence (non-photoconductive).

2.4. Photodetection Metrics and Optical Memory application

To characterize the NCFG phototransistor's performance as a light detector, the responsivity and detectivity were evaluated. Responsivity is a measure of the current generated from the incident optical power and can be determined by the equation:

$$R = I_{ph}/P_{opt} \quad (1)$$

where I_{ph} is the photocurrent (I_{LIGHT}-I_{DARK}) and P_{opt} is the effective optical power. In **Figure 4a**, the responsivity is shown at different gate biasing voltages. The highest responsivity achieved was 1.3x10^5 A/W for the minimum optical power density of 1.19 μW/cm^2. The trend for the responsivity decreases with increasing light intensities; however, for the lower gate bias, the responsivity started at a low value, peaked, and then decreased. This inverted parabolic trend arises from the lower photocurrent generated in comparison to the other higher gate biases. The detectivity describes the light sensor's sensitivity and can be determined from:

$$D^* = \frac{R\sqrt{A}}{\sqrt{2qIdark}} \quad (1)$$

where R is the responsivity, A is the area of the channel, q is the electronic charge, and I_{dark} is the dark current. The detectivity at varying optical power densities under different gate biases can be seen in Figure 4b. A peak detectivity of 7.2x10^{15} cm Hz$^{1/2}$ W^{-1} was obtained with the device biased at V_G = 0.175V (depletion mode). This bias point was selected, since $I_D > I_G$ at this operation point. At $V_G < V_{TH}$, the device is operated in the subthreshold region where the NC effect is supposed to occur. In the lower SS region, the dark current was as low as ~fA range. A comparison of detectivity among various device structures of MoS_2 photodetectors[3,7,35,36,37] is summarized in Figure 4c where this study offers the highest detectivity. Although the detectivity and responsivity are competing parameters, this NCFG device structure offers an opportunity to further suppress the dark current and enhances the photogating effect to increase its light sensitivity.

Optical memory functionality was explored with the NCFG monolayer MoS_2 phototransistor. Since the photocurrent generation mechanism process relies on the charge-trapping of the photogenerated holes tunneling into ZrO_2, the time response displays a long relaxation process which is known as the persistent photocurrent effect[28,29]. Although the charge-trapping process results in a slow time response, this feature can be useful for applications such as neuromorphic optical synapses or non-volatile optical memories. To explore the potential of this device as an optical memory, we tested multi-state programming and charge retention characteristics using weak light intensities since it can allow for a low-powered application. In Figure 4d, it shows the multi-state programming of three photocurrents generated from 3 different optical power densities. After the light pulse programming, the photocurrent remained stable for 100 seconds after light exposure. Next, its retention characteristics for 1000 second duration is found in Figure 4e where after the light pulse programming, the programmed photocurrent and the dark current (off-state) was measured. At the beginning, the programmed and off-state had a $\sim 10^2$ order of magnitude difference. After 1000 seconds, the difference decreased to ~10. Although it is common to introduce additional dielectric layers to improve the charge retention[30,31], this addition may impact the internal voltage amplification, so an appropriate design is needed. As for its use as a photodetector, the time response can be improved by applying a reset pulse to release the trapped charges as seen in supplementary figure 12 and 13. An interesting direction to further explore is the use of steep slope photodetectors capable of tuning between positive and negative photocurrent generation. 2D heterostructures seem to be a promising photoactive channel material to observe negative photocurrents, since the photogenerated charge transfer process can occur between the layers[43].

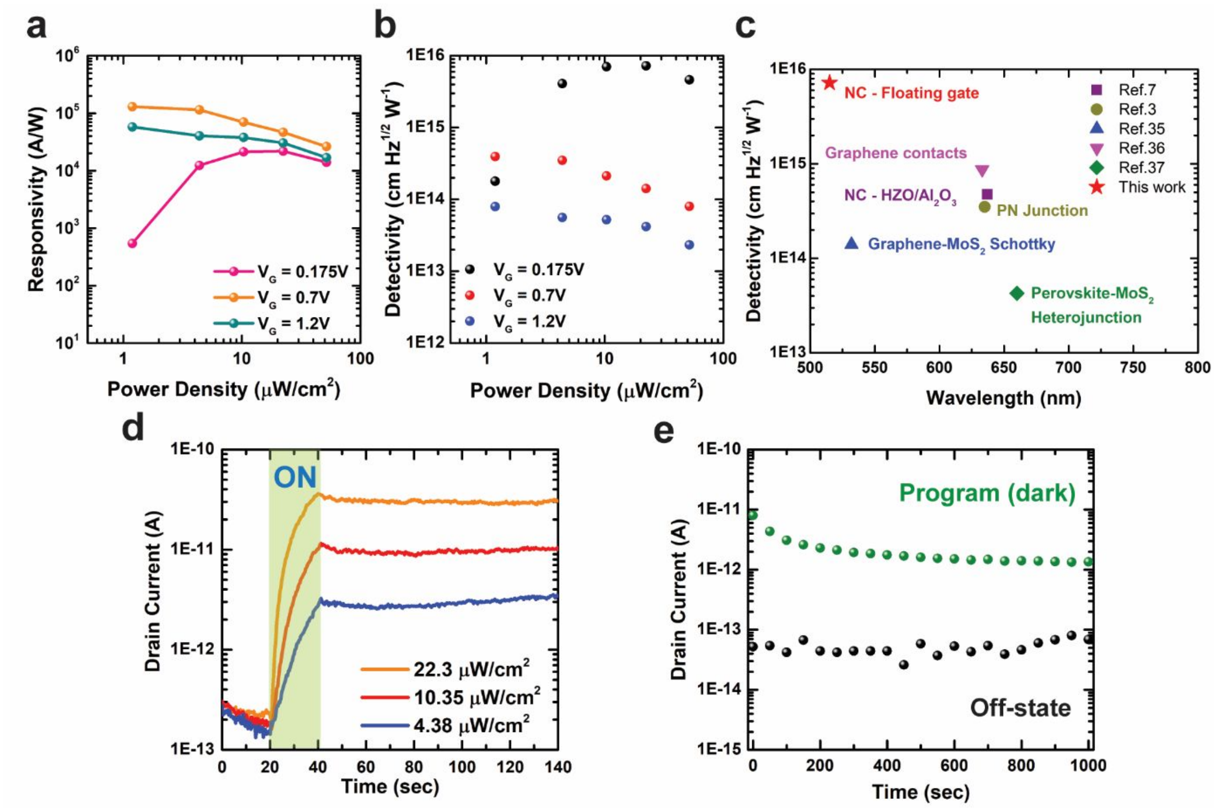

Figure 4. a) Responsivity vs. optical power density for different gate biases. b) Detectivity vs. optical power density for different gate biases. c) Benchmark of detectivity for different MoS_2 device structures. d) Multi-level photocurrent states after 20 second light pulse programming with V_{DS} = 100 mV and V_G = -150 mV. d) Optical memory retention of light current after light programming (green line) and the dark off-state (black line) with V_{DS} = 250 mV and V_G = -150 mV.

2.5. Optical Synapse and Artificial Neural Network

Neuromorphic computing systems are considered to be a possible future candidate to replace the conventional Von Neumann model utilized in current computing architectures. An efficient approach to build this system is the use of devices with built-in synaptic functionalities where one device represents a synapse. In particular, optical synaptic transistors can be used towards the development of neuromorphic vision systems where it can mimic the light sensing and initial processing that occur in the retina. A schematic overview can be seen in **Figure 5a** where phototransistors can be used to act as a transducer to convert light into an electronic signal. Neurons transmit information from the pre and post neurons via the release of neurotransmitters from the pre-neuron and its binding to the receptors on the post neuron. For optical synapse operation (Figure 5b), the pre-synaptic signal is provided by a short light pulse acting as an optical spike which generates the post-synaptic signal called the post-synaptic current (PSC). The synaptic weight can be determined from the connection strength between the pre and post neuron that can be modified via learning. The synaptic strength can be enhanced by long-term potentiation (LTP) and weakened by long-term depression (LTD). The LTP/LTD characteristics in Figure 5c shows the LTP by optical stimulation with green light pulses with an optical power density of 70 μW/cm^2, V_G = 0V, and V_{DS} = 150 mV. For LTD, electrical stimulation was used with V_G = -100 mV and V_{DS} = 150 mV for the read pulse since it is difficult to demonstrate optical depression (generating negative photocurrent). The LTP behavior showed linear-like conductance modulation which can be attributed to the PPC effect. Next, a NCFG artificial neural network (ANN) was simulated and its pattern recognition accuracy was tested using the MNIST handwriting dataset. The ANN[33] shown in Figure 5d consists of 400 input neurons, 100 hidden layer neurons, and 10 output neurons. Its recognition accuracy after 125 epochs in Figure 5e showed an accuracy of 87.8%. In comparison, the ideal performance had an accuracy of 92.6%.

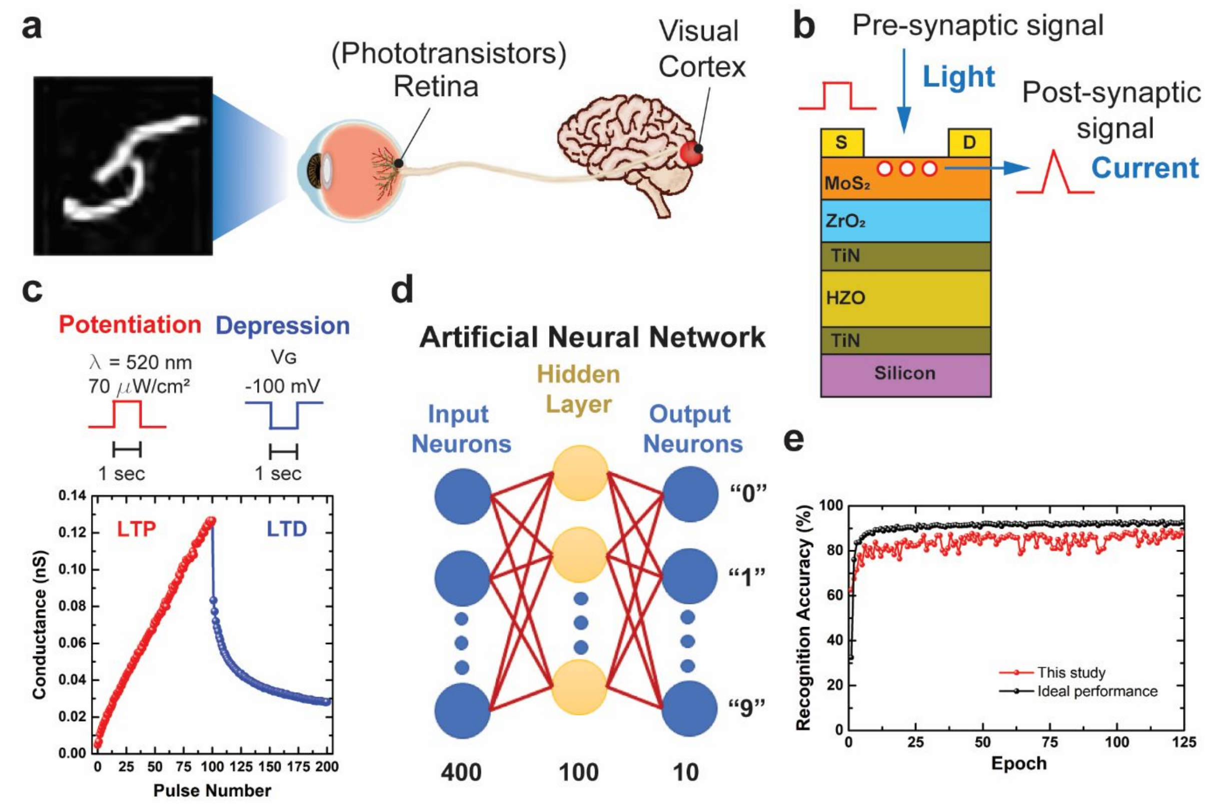

Figure 5. a) Schematic of neuromorphic vision system where phototransistor is used to mimic the functions of the retina. b) Device operation as an optical synapse. c) Long-term potentiation (LTP) by optical stimulation with $V_G = 0V$ and $V_{DS} = 150$ mV. Long-term depression (LTD) by electrical stimulation with $V_G = -100mV$ and $V_{DS} = 150$ mV for the read pulse. d) Schematic of the artificial neural network (ANN) used in the simulation for image recognition of MNIST handwriting dataset. The ANN consists of 400 input neurons, 100 hidden layer neurons, and 10 output neurons. e) ANN simulation results of the handwriting recognition accuracy. After 125 epochs, the NCFG neural network showed an accuracy of 87.8% and the ideal case was 92.6%.

3. Conclusion

In conclusion, a monolayer MoS_2 negative capacitance floating gate (NCFG) phototransistor device structure was investigated. This device structure contains a ferroelectric capacitor integrated with a conventional 2D FET which has potential for negative capacitance operation and also contains a floating gate. A strong photogating effect was observed that produced large threshold voltage shifting for weak light illumination. As a result, the highest detectivity among various MoS_2 photodetectors was achieved with a peak value of $7.2x10^{15}$ cm $Hz^{1/2}$ W^{-1} due to its enhancement in weak light detection in comparison to a conventional FET device structure. This device structure offers flexibility to transfer other kinds of 2D materials as photoactive channels to benefit from this enhanced photogating behavior. In addition, optical memory functionality of multi-state programming and charge retention was demonstrated for a duration of 1000 seconds. This device was also explored as an optical synapse where it displayed excellent long-term potentiation characteristics and was simulated in an artificial neural network (ANN). This NCFG ANN displayed an image pattern recognition accuracy of 87.8% after 125 epochs. Overall, the enhancement of photogenerated hole-trapping with this NCFG device structure allows for improved light sensitivity for weak light illumination.

4. Experimental Methods

Device Fabrication:

Heavily doped n-type Silicon was used as the substrate for the back gate. Next, DC sputtering of 50 nm of TiN was deposited and was followed by 11 nm of ALD deposited $Hf_{0.5}Zr_{0.5}O_2$ and then DC sputtering again with 30 nm of TiN. RTA post-metallization annealing at 700 °C was performed to achieve ferroelectricity. Next, ALD deposition of ZrO_2 at 300 °C with thickness of 11 nm. CVD monolayer MoS_2 purchased from SixCarbon Technology and was transferred onto ZrO_2 layer. Source/drain contacts were patterned using a photolithography process with channel length of 2.5 μm. Metal contacts of 10 nm Ti/ 70 nm Au was deposited by e-beam evaporation. Aluminum was deposited on the backside of Silicon to provide better electrical contact for the back gate, and then lift-off was performed.

Device Measurements:

All measurements were performed at room temperature and under ambient conditions with a dark curtain. A laser diode purchased from Thorlabs with wavelength of 515 nm was used for the photoresponse and optical memory measurements. A commercial LED with wavelength of 520 nm was used for the optical synapse measurements. Device measurements were performed using Cascade probe system (Form Factor) and Agilent 4156C Precision Semiconductor Parameter Analyzer. For a steady state condition for illumination measurements, the laser diode was on for ~1 minute before the measurement was taken. Agilent 33500B series waveform generator to provide the light pulse waveforms.

Supporting Information

Additional measurements (PDF).

Acknowledgements

This work was partly supported by JST CREST Grant Number JPMJCR1907 and partly supported by NIMS Joint Research Hub Program. This work was partly conducted at the Takeda Sentanchi Supercleanroom, The University of Tokyo, supported by "Nanotechnology Platform Program" of the Ministry of Education, Culture, Sports, Science and Technology (MEXT), Japan, Grant Number JPMXP09F-20-UT-0021. R.N. is supported by the Japanese Government Monbukagakusho (MEXT) scholarship. The authors would like to thank Mr. D. Nishioka from Tokyo University of Science for his assistance with the ANN simulation.

References

[1] S. Goossens, G. Navickaite, C. Monasterio, S. Gupta, J. Piqueras,R. Pérez, G. Burwell, I. Nikitskiy, T. Lasanta, T. Galán,E. Puma,A. Centeno, A. Pesquera, A. Zurutuza, G. Konstantatos, F. Koppens, *Nat Photon.* **2017**, *11*, 366.

[2] M. Kielar, H. Gooch, L. Xu, A.K. Pandey, P. Sah, *ACS Photonics.* **2021**, *8*, 228-237.

[3] N. Huo, G. Konstantatos, *Nat Commun.* **2017**, *8*, 1-6.

[4] I. Lee, W.T. Kang, J.E. Kim, Y.R. Kim, U.Y. Won, Y.H. Lee, W.J. Yu, *ACS Nano.* **2020**, *14*, 7574-7580.

[5] D. Kufer, T. Lasanta, M. Bernechea, F.H.L. Koppens, G. Konstantatos, *ACS Photonics.* **2016**, *3*, 1324-1330.

[6] S. Salahuddin, S. Dutta, *Nano Lett.* **2008**, *8*, 405-410.

[7] L. Tu, R. Cao, X. Wang, Y. Chen, S. Wu, F. Wang, Z. Wang, H. Shen, T. Lin, P. Zhou, X. Meng, W. Hu, Q. Liu, J. Wang, M. Liu, and J. Chu, *Nat Commun.* **2020**, *11*, 101.

[8] H. Li, Q. Zhang, C.C.R. Yap, B.K. Tay, T.H.T. Edwin, A. Olivier, D. Baillargeat, *Adv. Funct. Mater.* **2012**, *22*, 1385-1390.

[9] T. S. Boscke, J. Muller, D. Brauhaus, U. Schroder, U. Bottger, *Appl. Phys. Lett.* **2011**, *99*, 102903.

[10] J. Müller,T. S. Böscke,U. Schröder,S. Mueller,D. Brauhaus,U. Böttger, L. Frey, T. Mikolajick, *Nano Lett.* **2012**, *12*, 4318-4323.

[11] T. Olsen, U. Schröder, S. Müller, A. Krause, D. Martin, A. Singh, J. Müller, M. Geidel, T. Mikolajick, *Appl. Phys. Lett.* **2012**, *101*, 082905.

[12] S. Mueller, J. Mueller, A. Singh, S. Riedel, J. Sundqvist, U. Schroeder, T. Mikolajick, *Adv. Funct. Mater.* **2012**, *22*, 2412-2417.

[13] N. Setter, D. Damjanovic, L. Eng, G. Fox, S. Gevorgian, S. Hong, A. Kingon, H. Kohlstedt, N. Y. Park, G. B. Stephenson, I. Stolitchnov, A. K. Taganstev, D. V. Taylor, T. Yamada, S. Streiffer, *J. Appl. Phys.* **2006**, *100*, 051606.

[14] B. Neese, B. Chu, S.-G. Lu, Y. Wang, E. Furman, Q.M. Zhang, *Science.* **2008**, *321*, 821-823.

[15] M.H. Park, H.J. Kim, Y.J. Kim, W. Lee, T. Moon, C.S. Hwang, *Appl. Phys. Lett.* **2013**, *102*, 242905.

[16] M.H. Park, H.J. Kim, Y.J. Kim, W. Lee, T. Moon, K.D. Kim, C.S. Hwang, *Appl. Phys. Lett.* **2014**, *105*, 072902.

[17] G. Pahwa, T. Dutta, A. Agarwal,S. Khandelwal, S. Salahuddin, C. Hu, Y.S. Chauhan, *IEEE Trans. Electron Devices.* **2016**, *63*, 4986-4992.

[18] T. Yu, W. Lü, Z. Zhao, P. Si, K. Zhang, *Microelectron. J.* **2021**, *108*, 104981.

[19] M. Buscema, J.O. Island, D.J. Groenendijk, S.I. Blanter, G.A. Steele, H.S.J. van der Zant, A. Castellanos-Gomez, *Chem. Soc. Rev.* **2015**, *44*, 3691.

[20] R. Nur, T. Tsuchiya, K. Toprasertpong, K. Terabe, S. Takagi, M. Takenaka, *Commun. Mater.* **2020**, *103*, 1.

[21] F. Liao, J. Deng, X. Chen, Y. Wang, X. Zhang, J. Liu, H. Zhu, L. Chen, Q. Sun, W. Hu, J. Wang, J. Zhou, P. Zhou, D.W. Zhang, J. Wan, W. Bao, *Small.* **2020**, *16*, 1904369.

[22] J.-Y. Wu, Y. T. Chun, S. Li, T. Zhang, J. Wang, P.K. Shrestha, D. Chu, *Adv. Mater.* **2018**, *30*, 1705880.

[23] A.S. Foster, V.B. Sulimov, F. Lopez Gejo, A.L. Shluger, R. M. Nieminen, *Phys. Rev. B.* **2001**, *64*, 224108.

[24] T.V. Perevalov, D.R. Islamov, *Microelectron. Eng.* **2017**, *178*, 275.

[25] J.R. Chavez, R.A.B. Devine, L. Koltunski, *J. Appl. Phys.* **2001**, *90*, 4284.

[26] P. Han, E.R. Adler, Y. Liu, L. St Marie, A. El Fatimy,S. Melis, E. Van Keuren, P. Barbara, *Nanotechnology.* **2019**, *30*, 284004.

[27] H. Fang, W. Hu, *Adv. Sci.* **2017**, *4*, 1700323.

[28] A. Di Bartolomeo, L. Genovese1, T. Foller, F. Giubileo, G. Luongo, L. Croin, S.-J. Liang, L.K. Ang, M. Schleberger, *Nanotechnology.* **2017**, *28*, 214002.

[29] Y.-C. Wu, C.-H. Liu, S.-Y. Chen, F.-Y. Shih, P.-H. Ho, C.-W. Chen, C.-T. Liang, W.-H. Wang, *Sci. Rep.* **2015**, *5*, 1-10.

[30] K. Agrawal, G. Yoon, J. Kim, G. Chavan, J. Kim, J. Park, P.D. Phong, E.-C. Cho, J. Yi, *ECS J. Solid State Sci.* **2020**, *9*, 043002.

[31] P.-H. Tsai, K.-S. Chang-Liao, T.-C. Liu, T.-K. Wang, P.-J. Tzeng, C.-H. Lin, L. S. Lee, M.-J. Tsai, *IEEE Electron Device Lett.* **2009**, *30*, 775-777.

[32] F. A. McGuire, Y.-C. Lin, K. Price, G. B. Rayner, S. Khandelwal, S. Salahuddin, A. D. Franklin, *Nano Lett*. **2017**, 17, 4801-4806.

[33] P.-Y. Chen, X. Peng, S. Yu, IEEE International Electron Devices Meeting (IEDM), pp. 6.1.1-6.1.4, 2017.

[34] C. Chang, S. Haddad, B. Swaminathan, J. Lien, IEEE Electronic Device Letters. **1988**, 9, 588-590.

[35] W. Deng, Y. Chen, C. You, B. Liu, Y. Yang, G. Shen, S. Li, L. Sun, Y. Zhang, H. Yan, Adv. Electron. Mater. 2018, 4, 1800069.

[36] P. Han, L. St. Marie, Q.X. Wang, N. Quirk, A. El Fatimy, M. Ishigami, P. Barbara, Nanotechnology, 2018, 29, 20LT01.

[37] Z.Y. Peng, J.-L. Xu, J.-Y. Zhang, X. Gao, S.-D. Wang, Adv. Mater. Interfaces, 2018, 5, 1800505.

[38] K.F. Mak, C. Lee, J. Hone, J. Shan, T.F. Heinz, *Phys. Rev. Lett.* **2010**, *105*, 136805.

[39] S. Tongay, H. Sahin, C. Ko, A. Luce, W. Fan, K. Liu, J. Zhou, Y.-S. Huang, C.-H. Ho, J. Yan, D. F. Ogletree, S. Aloni, J. Ji, S. Li, J. Li, F.M. Peeters, J. Wu, *Nat Commun.* **2014**, *5*, 1-6.

[40] G.W. Mudd, M.R. Molas, X. Chen, V. Zólyomi, K. Nogajewski, Z.R. Kudrynskyi, Z.D. Kovalyuk, G. Yusa, O. Makarovsky, L. Eaves, M. Potemski, V. I. Fal'ko, A. Patanè, *Sci Rep.* **2016**, *6*, 39619.

[41] F. Urban, F. Giubileo, A. Grillo, L Iemmo, G. Luongo, M. Passacantando, T. Foller, L. Madauß, E. Pollmann, M. P. Geller, D. Oing, M. Schleberger, A. Di Bartolomeo, *2D Mater.* 2019, 6, 045049.

[42] F. Giubileo, L. Iemmo, M. Passacantando, F. Urban, G. Luongo, L. Sun, G. Amato, E. Enrico, A. Di Bartolomeo, *J. Phys. Chem. C* 2019, 123, 2, 1454–1461.

[43] Y. Wang, E. Liu, A. Gao, T. Cao, M. Long, C. Pan, L. Zhang, J. Zeng, C. Wang, W. Hu, S.-J. Liang, F. Miao, *ACS Nano* 2018, 12, 9, 9513–9520.